(Preprint) AAS 24-270

A NUMERICAL METHOD FOR COMPUTING THE STATE TRANSITION MATRIX USING POINCARÉ INTEGRAL INVARIANTS

Michael A. Shoemaker* **and Kyle M. Hughes†**

The Poincaré integral invariants describe the volumes of sets in Hamiltonian phase space. We use these invariants to derive a new numerical procedure for obtaining the state transition matrix (STM), which can be applied to both conservative and nonconservative systems. The method is analogous to a finite difference approximation of the STM, where perturbed states are numerically propagated along with the reference trajectory. We discuss the mathematical similarities between this new STM and existing methods, show numerical results for orbital motion and uncertainty propagation, and discuss new insights afforded by the Hamiltonian properties of phase flow.

INTRODUCTION

Many problems in dynamical systems theory, trajectory optimization, estimation and uncertainty propagation require a state transition matrix (STM), $\mathbf{\Phi}$. This paper introduces a new method for computing $\mathbf{\Phi}$ which proceeds geometrically from Liouville's theorem and the Poincaré integral invariants. The method is analogous to a forward finite difference approximation of the STM, in that test particle trajectories are numerically propagated along with the reference trajectory in order to form $\mathbf{\Phi}$ at a given time.

Pellegrini[1] is a handy paper that discusses many different ways to compute STMs and their comparisons. Probably the most standard way of solving for the STM is to integrate the variational equations along with the reference trajectory. This method is accurate if one has written the partial derivatives of the accelerations. Numerical approaches, such as a finite difference approximation, are attractive in that they don't require analytical expressions for the partial derivatives, but they can suffer from accuracy issues. One benefit of a numerical approach such as a finite difference is the force model in the orbit propagator can be treated as a black box. The desire to improve on such black-box approaches was one motivation for pursuing this research.

Within the astrodynamics community there has been recent interest in studying the Poincaré integral invariants. Scheeres et al.[2,3] and Boodram and Scheeres[4] used the invariants to study fundamental limits on spacecraft uncertainty distributions. Other research has looked into constraining the evolution of uncertainty using control laws that leverage the integral invariants.[5] To our knowledge this work represents the first application of the Poincaré integral invariants to deriving an STM.

*Aerospace Engineer, Navigation and Mission Design Branch, NASA Goddard Space Flight Center, Greenbelt, MD, 20771, USA.

†Aerospace Engineer, Navigation and Mission Design Branch, NASA Goddard Space Flight Center, Greenbelt, MD, 20771, USA.

BACKGROUND

Let the Hamiltonian system in question have n degrees of freedom (DOF), with generalized coordinates $\mathbf{q} = (q_i; i = 1, n)$ and conjugate momenta $\mathbf{p} = (p_i; i = 1, n)$. The state of the system is $\mathbf{x} = [\ \mathbf{q}\ \ \mathbf{p}\ ]^T$, where $\mathbf{x} \in \mathbb{R}^{2n}$. Given some initial conditions, the motion of the system is uniquely described by Hamilton's equations:

$$\dot{\mathbf{x}} = J\frac{\partial H}{\partial \mathbf{x}} \tag{1}$$

$$J \equiv \begin{bmatrix} \mathbf{O}_n & \mathbf{I}_n \\ -\mathbf{I}_n & \mathbf{O}_n \end{bmatrix} \tag{2}$$

where $H(\mathbf{q}, \mathbf{p}, t)$ is the Hamiltonian, and $\mathbf{O}_n$ and $\mathbf{I}_n$ are the $n \times n$ zero and identity matrices, respectively. The resulting motion $\mathbf{x}(t)$ is represented geometrically by trajectories in phase space of dimension $\mathbb{R}^{2n}$.

For the $n = 3$ DOF problems of interest in astrodynamics, we are concerned with the 6-dimensional state $\mathbf{x}$ having position and velocity. A spacecraft under conservative gravitational forces has Lagrangian $L(\mathbf{q}, \dot{\mathbf{q}})$ written using the kinetic (T) and potential (V) energies:

$$L(\mathbf{q}, \dot{\mathbf{q}}) = T(\mathbf{q}, \dot{\mathbf{q}}) - V(\mathbf{q}) \tag{3}$$

where $(q_1, q_2, q_3) = (x, y, z)$, $T = m\dot{\mathbf{q}}^T\dot{\mathbf{q}}/2$, and $V = -\mu/\|\mathbf{q}\|$. The conjugate momenta are defined by $p_i = \partial L/\partial \dot{q}_i$, and thus

$$p_1 = \partial L/\partial \dot{x} = m\dot{x} \tag{4}$$

$$p_2 = \partial L/\partial \dot{y} = m\dot{y} \tag{5}$$

$$p_3 = \partial L/\partial \dot{z} = m\dot{z} \tag{6}$$

Poincaré Integral Invariants

This paper does not attempt to re-derive the Poincaré integral invariants*; instead the reader is directed to the excellent discussions in Arnold,[7] Scheeres,[2] and Boodram,[4] among others.

Let $\mathcal{B}_n$ be an n-dimensional distribution or set of points in phase space:

$$\mathcal{B}_n = \{\mathbf{x} | \mathbf{x} \in M^n \subset \mathbb{R}^{2n}\} \tag{7}$$

where the set M^n is a closed and connected manifold having dimension n. The well-known Liouville's theorem, which is covered in most undergraduate-level textbooks on classical mechanics, states that a conservative Hamiltonian system will preserve phase space volume, although the shape of the volume may deform with time (see Fig. 1). Therefore, if we were to compute the volume of the set $\mathcal{B}_n$ at two different times, that volume would be constant. Conversely, a nonconservative system will not preserve phase space volume.

Liouville's theorem is actually a generalization of the Poincaré integral invariants, which are explained in words as: for the set $\mathcal{B}_n$, the sum of the oriented areas of the set's orthogonal projections

*These integral invariants are often attributed to either Poincaré or Poincaré-Cartan in the literature. We follow the convention described in Jordan[6] and Arnold,[7] where a Poincaré-Cartan integral invariant refers to $\oint \mathbf{p}d\mathbf{q} - Hdt$, and a Poincaré integral invariant refers to the same quantity when the term Hdt is absent. As will become clear below, we consider phase-space states at a constant time t, and thus $dt = 0$.

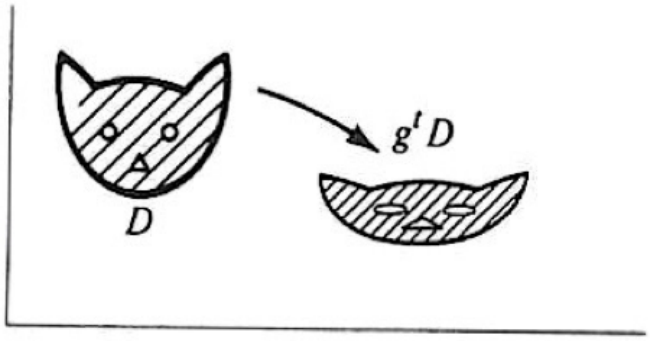

Figure 1. A cartoon reproduced from Arnold[7] with an exceptionally cute representation of Liouville's theorem. The cat on the left is a set of points in phase space at an initial time; the cat on the right shows the deformed state (with equal volume) at a later time.

onto all non-intersecting canonical conjugate planes is invariant for Hamiltonian phase flow. To use the description in Scheeres:[2] a quantity is an integral invariant if the integration of an arbitrary set $\mathcal{B}_{2k}$ is conserved when summed over all possible symplectic combinations of degree $2k$. The term "symplectic combination" or "symplectic pair" means the pair of generalized coordinates and conjugate momenta (q_i, p_i) that correspond with each other.

The simplest example of a Poincaré integral invariant, and the one we will focus on the most, is for 2-dimensional sets $\mathcal{B}_2$. This invariant is written as

$$I_2(t) = \sum_{i=1}^{n} \int_{\mathcal{B}_2(t)} dq_i \wedge dp_i \tag{8}$$

$$= I_2(\tau) \; \forall \; \tau \; \in \mathbb{R} \tag{9}$$

Given the current $n = 3$ DOF problem, Eq. 8 becomes

$$I_2(t) = \int_{\mathcal{B}_2(t)} dq_1 \wedge dp_1 + \int_{\mathcal{B}_2(t)} dq_2 \wedge dp_2 + \int_{\mathcal{B}_2(t)} dq_3 \wedge dp_3 \tag{10}$$

Figure 2 shows an illustration of an arbitrary 6-dimensional hypervolume of the set $\mathcal{B}_6$, which has been projected into the three orthogonal subspaces in $\mathcal{B}_2$. Later we will be comparing the integral invariants at two different points in time; if we assume constant spacecraft mass, from Eqs. 4 to 6, then we can drop m and replace the notation of (q_i, p_i) with the cartesian position and velocity components for convenience.

The integrand in Eq. 8 is the exterior product of the differential elements over the surface. The exterior product preserves the sign of the area (i.e. the *oriented* area), and is analogous to the cross product in computing the area of a parallelogram with sides dp_i and dq_i. This is important, because the oriented area from each subspace projection in Eq. 8 may be positive or negative, but the final sum in I_2 will be invariant.

For $n = 3$, there are two other Poincaré integral invariants, I_4 and I_6. The invariant I_4 has similar form as Eq. 8, but the integral is over the $\mathcal{B}_4$ subspace projections:

$$I_4(t) = \int_{\mathcal{B}_4(t)} dq_1 \wedge dp_1 \wedge dq_2 \wedge dp_2 + \int_{\mathcal{B}_4(t)} dq_2 \wedge dp_2 \wedge dq_3 \wedge dp_3 + \int_{\mathcal{B}_4(t)} dq_3 \wedge dp_3 \wedge dq_1 \wedge dp_1 \tag{11}$$

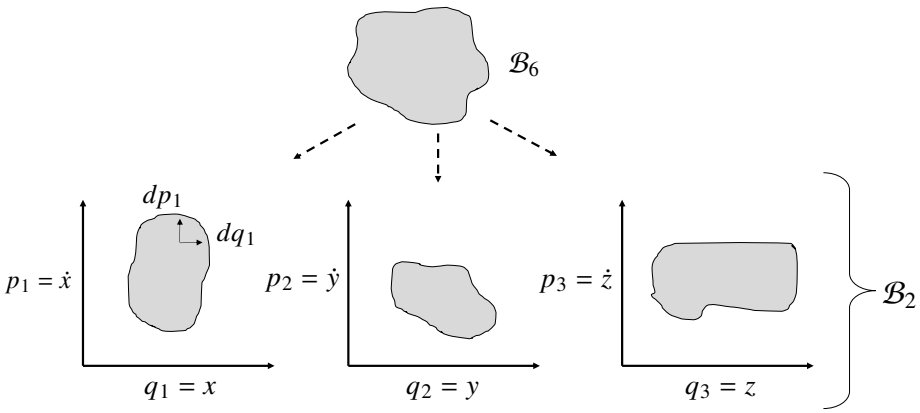

Figure 2. Illustration of a 6-dimensional hypervolume being projected in the 2-dimensional subspaces of symplectic pairs, for the case of $n = 3$ cartesian position and velocity.

I_6 is equivalent to the standard Liouville's theorem concerning the volume over the set $\mathcal{B}_6$:

$$I_{2n}(t) = \int_{\mathcal{B}_{2n}(t)} dq_1 \wedge dp_1 \wedge \ldots \wedge dq_n \wedge dp_n \tag{12}$$

which for $n = 3$ becomes

$$I_6(t) = \int_{\mathcal{B}_6(t)} dq_1 \wedge dp_1 \wedge dq_2 \wedge dp_2 \wedge dq_3 \wedge dp_3 \tag{13}$$

We will mostly ignore I_4 and I_6 for the remainder of this memo, for reasons that will become apparent shortly. Before moving on, let's introduce the following notation for Eq. 8 that will come in handy:

$$I_2 = A_{x\dot{x}} + A_{y\dot{y}} + A_{z\dot{z}} \tag{14}$$

showing clearly that we are summing the areas of the subspace projections for each of the symplectic pairs.

Computing Volume

It is now necessary to discuss the computation of volume in Euclidian geometry of various dimensions. Although Fig. 2 shows our sets $\mathcal{B}_n$ as amorphous blobs, the STM derivation to follow will use sets of k-simplexes. A k-simplex is a k-dimensional polytope, which is a convex hull of its $k + 1$ vertices. For example, a 0-simplex is a point, a 1-simplex is a line segment, a 2-simplex is a triangle, a 3-simplex is a tetrahedron, etc. In other words, a k-simplex is the smallest convex set containing the vertices.

It turns out that a k-simplex has an easy formula for its *oriented* volume*:

$$\text{volume} = \frac{1}{k!} \det \begin{bmatrix} \mathbf{v}_1 & \cdots & \mathbf{v}_{k+1} \\ 1 & \cdots & 1 \end{bmatrix} \tag{15}$$

where $\mathbf{v}_i$ is the i-th k-dimensional vertex of the k-simplex. The determinant in Eqn. 15 is a multilinear function, meaning that for a given vertex $\mathbf{v}_i$, the equation is linear in $\mathbf{v}_i$.

*Meaning we drop the absolute value that normally appears here, and accept the fact that the volume could be positive or negative depending on the ordering of the vertices in Eq. 15

NEW STM DERIVATION USING I_2

The new STM is derived using the I_2 Poincaré integral invariant and the multilinear property of the determinant. The derivation is similar to a forward finite difference method, in that several test particles are propagated in additional to the reference trajectory. Consider at an initial time t_0 the true state $\mathbf{x}(t_0)$, the reference state $\mathbf{x}^*(t_0)$ about which the linearization is performed, and some test particle $\mathbf{x}_i(t_0)$. As Fig. 3 illustrates, these three states will enclose a triangle (denoted in green) in each of the three symplectic pair subspaces in $\mathcal{B}_2$.

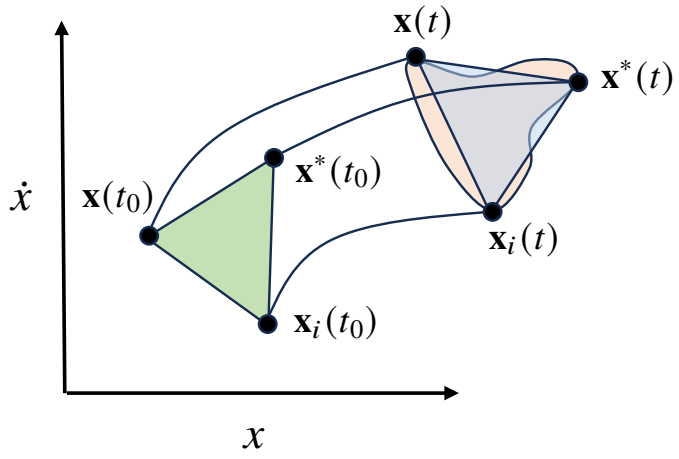

Figure 3. Illustration of truth ($\mathbf{x}$), reference ($\mathbf{x}^*$), and i-th test particle ($\mathbf{x}_i$) trajectories in phase space, showing one subspace projection for the symplectic pair x and $\dot{x}$.

For now, let's restrict the discussion to the 2-dimensional subspace for the symplectic pair x and $\dot{x}$. Let's also drop the time dependence since that will be made clear later. Let the vertices of the 2-simplex (*i.e.* triangle) in Eqn. 15 be represented relative to the reference trajectory:

$$\mathbf{v}_1 = \begin{bmatrix} x^* - x^* \\ \dot{x}^* - \dot{x}^* \end{bmatrix} = \begin{bmatrix} 0 \\ 0 \end{bmatrix} \tag{16}$$

$$\mathbf{v}_2 = \begin{bmatrix} x_i - x^* \\ \dot{x}_i - \dot{x}^* \end{bmatrix} = \begin{bmatrix} \delta x_i \\ \delta \dot{x}_i \end{bmatrix} \tag{17}$$

$$\mathbf{v}_3 = \begin{bmatrix} x - x^* \\ \dot{x} - \dot{x}^* \end{bmatrix} = \begin{bmatrix} \delta x \\ \delta \dot{x} \end{bmatrix} \tag{18}$$

Then the area (or volume) of the subspace projections are found by evaluating the determinant in Eqn. 15 for the k-simplex in each of the three subspaces*:

$$A_{x\dot{x}} = \begin{bmatrix} -\delta \dot{x}_i & \delta x_i \end{bmatrix} \begin{bmatrix} \delta x \\ \delta \dot{x} \end{bmatrix} \tag{19}$$

$$A_{y\dot{y}} = \begin{bmatrix} -\delta \dot{y}_i & \delta y_i \end{bmatrix} \begin{bmatrix} \delta y \\ \delta \dot{y} \end{bmatrix} \tag{20}$$

*The term $1/k!$ can be dropped, because it will cancel out later anyway.

$$A_{z\dot{z}} = \begin{bmatrix} -\delta\dot{z}_i & \delta z_i \end{bmatrix} \begin{bmatrix} \delta z \\ \delta\dot{z} \end{bmatrix} \tag{21}$$

where we've used the multilinear property of the determinant to write the areas as a linear function of $\delta\mathbf{x}$.

The Poincaré integral invariant from Eqn 14 for the i-th test particle trajectory is then found from summing Eqs. 19 to 21:

$$I_{2_i} = A_{x\dot{x}} + A_{y\dot{y}} + A_{z\dot{z}} \tag{22}$$

$$= \begin{bmatrix} -\delta\dot{x}_i & -\delta\dot{y}_i & -\delta\dot{z}_i & \delta x_i & \delta y_i & \delta z_i \end{bmatrix} \begin{bmatrix} \delta x \\ \delta y \\ \delta z \\ \delta\dot{x} \\ \delta\dot{y} \\ \delta\dot{z} \end{bmatrix} \tag{23}$$

Defining the terms $\delta\mathbf{r} \equiv \begin{bmatrix} \delta x & \delta y & \delta z \end{bmatrix}^T$ and $\delta\mathbf{v} \equiv \begin{bmatrix} \delta\dot{x} & \delta\dot{y} & \delta\dot{z} \end{bmatrix}^T$, Eq. 23 is written as

$$I_{2_i} = \begin{bmatrix} -\delta\mathbf{v}_i^T & \delta\mathbf{r}_i^T \end{bmatrix} \begin{bmatrix} \delta\mathbf{r} \\ \delta\mathbf{v} \end{bmatrix} \tag{24}$$

If we then consider N test particles, where $N = 2n$, we can construct the following from Eq. 24:

$$\begin{bmatrix} I_{2_i} \\ \vdots \\ I_{2_N} \end{bmatrix} = \begin{bmatrix} -\delta\mathbf{v}_i^T & \delta\mathbf{r}_i^T \\ \vdots & \vdots \\ -\delta\mathbf{v}_N^T & \delta\mathbf{r}_N^T \end{bmatrix} \begin{bmatrix} \delta\mathbf{r} \\ \delta\mathbf{v} \end{bmatrix}, \qquad i = 1, \ldots, N \tag{25}$$

We can rewrite Eq. 25 with the matrix notation

$$\mathbf{y} = \mathbf{\Omega}\delta\mathbf{x} \tag{26}$$

where $\mathbf{y} \equiv \begin{bmatrix} I_{2_i} & \ldots & I_{2_N} \end{bmatrix}^T$, $\delta\mathbf{x} \equiv \begin{bmatrix} \delta\mathbf{r}^T & \delta\mathbf{v}^T \end{bmatrix}^T$ and

$$\mathbf{\Omega} \equiv \begin{bmatrix} -\delta\mathbf{v}_i^T & \delta\mathbf{r}_i^T \\ \vdots & \vdots \\ -\delta\mathbf{v}_N^T & \delta\mathbf{r}_N^T \end{bmatrix} \tag{27}$$

The derivation up to this point has considered all quantities at the initial time t_0. Let us now introduce a time dependence, and frame the discussion from the standpoint of solving for the state of interest $\delta\mathbf{x}(t)$. The left hand side of Eq. 26 contains the I_2 integral invariants for each of the $i \in 1, \ldots, N$ sets of k-simplex points, which by definition is constant in time. Thus,

$$\mathbf{y} = \mathbf{\Omega}(t_0)\delta\mathbf{x}(t_0) = \mathbf{\Omega}(t)\delta\mathbf{x}(t) + \boldsymbol{\epsilon} \tag{28}$$

where $\boldsymbol{\epsilon}$ represents an error term that can be visualized in Fig. 3. The set $\mathcal{B}_2$ is initially a perfect triangle (green), and therefore its area can be represented by the area of the three nodes in the triangle, but as the system is propagated forward in time the locus of points in the set turns into the region (orange) and can no longer be exactly represented by a triangle (blue). If we neglect the error $\boldsymbol{\epsilon}$, then we can simply solve for the state deviation $\delta\mathbf{x}(t)$ using our knowledge of the initial

conditions at t_0 and the $N+1$ trajectories (*i.e.* N test particles and one reference trajectory) that have been propagated to t using

$$\delta\mathbf{x}(t) = \mathbf{\Omega}^{-1}(t)\mathbf{\Omega}(t_0)\delta\mathbf{x}(t_0) \tag{29}$$

We assume that $\mathbf{\Omega}(t)$ is invertible because it is square (i.e. by earlier setting $N = 2n$) and by judicious choice of the reference trajectories*. It is now apparent that Eq. 29 is in the form of a linearized mapping of the state deviation vector from t_0 to t, and can thus be written as a STM:

$$\delta\mathbf{x}(t) = \mathbf{\Phi}_P(t, t_0)\delta\mathbf{x}(t_0) \tag{30}$$

where

$$\mathbf{\Phi}_P(t, t_0) \equiv \mathbf{\Omega}^{-1}(t)\mathbf{\Omega}(t_0) \tag{31}$$

The subscript P is to denote it as the STM derived using the Poincaré integral invariants, because it will be compared with other STMs later. It is straightforward to show that this new STM satisfies the identity, inverse, and commutative properties we come to expect from an STM (see Appendix A). Note that the times t_0 and t are meant to be general; when we apply the method we will replace these with the integration time steps t and $t + \Delta t$.

DISCUSSION

Before showing some numerical experiments to test this new method, it is worthwhile to discuss some options.

Defining Test Particles

We need to define $N = 6$ test particle initial conditions at t_0, and the inverse $\mathbf{\Omega}^{-1}(t)$ must exist. We have room to play some games here. In general, any arbitrary test particles can be defined by randomly perturbing the reference trajectory to yield $\delta\mathbf{x}_i(t_0)$, and likewise $\mathbf{\Omega}(t_0)$ through Eq. 27. One just needs to propagate the test particles to time t and hope that the matrix $\mathbf{\Omega}^{-1}(t)$ is invertible. We show below that judicious choice of test particles allows us to guarantee that this matrix inverse exists. Let us consider two options, written below in terms of $\mathbf{\Omega}(t_0)$:

- Case A:

$$\mathbf{\Omega}(t_0) = \begin{bmatrix} 0 & 0 & 0 & \delta x_1(t) & 0 & 0 \\ 0 & 0 & 0 & 0 & \delta y_2(t) & 0 \\ 0 & 0 & 0 & 0 & 0 & \delta z_3(t) \\ -\delta\dot{x}_4(t) & 0 & 0 & 0 & 0 & 0 \\ 0 & -\delta\dot{y}_5(t) & 0 & 0 & 0 & 0 \\ 0 & 0 & -\delta\dot{z}_6(t) & 0 & 0 & 0 \end{bmatrix} \tag{32}$$

- Case B:

$$\mathbf{\Omega}(t_0) = \mathrm{diag}\left(\begin{bmatrix} -\delta\dot{x}_1(t_0) & -\delta\dot{y}_2(t_0) & -\delta\dot{z}_3(t_0) & \delta x_4(t_0) & \delta y_5(t_0) & \delta z_6(t_0) \end{bmatrix}\right) \tag{33}$$

*We will return to this point soon.

Case A is a natural starting point, because the first test particle perturbs x, the next perturbs y, and so on. Case B might not be an obvious choice, but this case is shown in the next section to be equivalent to the forward finite difference approach.

We now show that both Cases A and B allow the matrix inverse $\mathbf{\Omega}^{-1}(t)$ to exist and to be evaluated without needing to numerically perform the inversion. For Case A, let Eq. 32 be written as

$$\mathbf{\Omega}(t_0) = \begin{bmatrix} \mathbf{0} & \mathbf{R} \\ \mathbf{V} & \mathbf{0} \end{bmatrix} \tag{34}$$

where $\mathbf{R} \equiv \text{diag}\left(\begin{bmatrix} \delta r_1 & \delta r_2 & \delta r_3 \end{bmatrix}\right)$ and $\mathbf{V} \equiv \text{diag}\left(\begin{bmatrix} -\delta v_4 & -\delta v_5 & -\delta v_6 \end{bmatrix}\right)$, and $\mathbf{0}$ and $\mathbf{I}$ are the 3×3 zero and identity matrices, respectively. Eq. 34 can be rewritten as

$$\mathbf{\Omega}(t_0) = \begin{bmatrix} \mathbf{I} & \mathbf{0} \\ \mathbf{0} & \mathbf{V} \end{bmatrix} \begin{bmatrix} \mathbf{0} & \mathbf{I} \\ \mathbf{I} & \mathbf{0} \end{bmatrix} \begin{bmatrix} \mathbf{I} & \mathbf{0} \\ \mathbf{0} & \mathbf{R} \end{bmatrix} \tag{35}$$

Noting that the matrix $\begin{bmatrix} \mathbf{0} & \mathbf{I} \\ \mathbf{I} & \mathbf{0} \end{bmatrix}$ is orthogonal, the inverse of Eq. 35 reduces to

$$\mathbf{\Omega}^{-1}(t_0) = \begin{bmatrix} \mathbf{I} & \mathbf{0} \\ \mathbf{0} & \mathbf{R} \end{bmatrix}^{-1} \begin{bmatrix} \mathbf{0} & \mathbf{I} \\ \mathbf{I} & \mathbf{0} \end{bmatrix}^{T} \begin{bmatrix} \mathbf{I} & \mathbf{0} \\ \mathbf{0} & \mathbf{V} \end{bmatrix}^{-1} = \begin{bmatrix} \mathbf{0} & \mathbf{V}^{-1} \\ \mathbf{R}^{-1} & \mathbf{0} \end{bmatrix} \tag{36}$$

From Eq. 52 in Appendix A, we show that

$$\mathbf{\Phi}_P^{-1}(t, t_0) = \mathbf{\Omega}^{-1}(t_0)\mathbf{\Omega}(t) \tag{37}$$

which, when combined with Eq. 36, results in

$$\mathbf{\Phi}_P^{-1}(t, t_0) = \mathbf{\Omega}^{-1}(t_0)\mathbf{\Omega}(t) \tag{38}$$

$$= \begin{bmatrix} \mathbf{0} & \mathbf{V}^{-1} \\ \mathbf{R}^{-1} & \mathbf{0} \end{bmatrix} \begin{bmatrix} \mathbf{\Omega}_{11} & \mathbf{\Omega}_{12} \\ \mathbf{\Omega}_{21} & \mathbf{\Omega}_{22} \end{bmatrix} \tag{39}$$

$$= \begin{bmatrix} \mathbf{V}^{-1}\mathbf{\Omega}_{21} & \mathbf{V}^{-1}\mathbf{\Omega}_{22} \\ \mathbf{R}^{-1}\mathbf{\Omega}_{11} & \mathbf{R}^{-1}\mathbf{\Omega}_{12} \end{bmatrix} \tag{40}$$

where we've introduced a shorthand notation for the 3×3 block elements of $\mathbf{\Omega}(t)$:

$$\mathbf{\Omega}(t) = \begin{bmatrix} \mathbf{\Omega}_{11} & \mathbf{\Omega}_{12} \\ \mathbf{\Omega}_{21} & \mathbf{\Omega}_{22} \end{bmatrix} \tag{41}$$

Recall that we've approximated our system as a conservative Hamiltonian system between times t_0 and t. Because the STM is symplectic for a conservative Hamiltonian system, $\mathbf{\Phi}_P^{-1}(t, t_0)$ can be decomposed into 3×3 block components[8]

$$\mathbf{\Phi}_P^{-1}(t, t_0) = \begin{bmatrix} \mathbf{\Phi}_{vv}^T & -\mathbf{\Phi}_{rv}^T \\ -\mathbf{\Phi}_{vr}^T & \mathbf{\Phi}_{rr}^T \end{bmatrix} \tag{42}$$

which can be rearranged to recover the STM without performing a matrix inversion:

$$\mathbf{\Phi}_P(t, t_0) = \begin{bmatrix} \mathbf{\Phi}_{rr} & \mathbf{\Phi}_{rv} \\ \mathbf{\Phi}_{vr} & \mathbf{\Phi}_{vv} \end{bmatrix} \tag{43}$$

where Eq. 40 is simple to evaluate, with $\mathbf{R}^{-1} = \text{diag}\left(\begin{bmatrix} \delta r_1^{-1} & \delta r_2^{-1} & \delta r_3^{-1} \end{bmatrix}\right)$ and $\mathbf{V}^{-1} = \text{diag}\left(\begin{bmatrix} -\delta v_4^{-1} & -\delta v_5^{-1} & -\delta v_6^{-1} \end{bmatrix}\right)$. A similar argument can be made for Case B: recalling Eq. 33, the inverse $\mathbf{\Omega}^{-1}(t_0)$ is trivial to compute because $\mathbf{\Omega}(t_0)$ is a diagonal matrix, and the rest of the derivation follows as already shown from Eqs. 37, 42 and 43.

Comparison with Forward Finite Difference

The new state transition matrix $\mathbf{\Phi}_P$ can be shown to be equivalent to one obtained with the forward finite difference method (i.e. difference quotient approximation) in Case B defined above. The STM from a forward finite difference method, denoted by $\mathbf{\Phi}_{FD}$ is found by perturbing the reference state at t_0 in each of the six components individually, and computing the sensitivity matrix as follows:

$$\mathbf{\Phi}(t,t_0) = \frac{\partial \mathbf{x}(t)}{\partial \mathbf{x}(t_0)} \approx \begin{bmatrix} \frac{\delta x(t)}{\delta x(t_0)} & \frac{\delta x(t)}{\delta y(t_0)} & \frac{\delta x(t)}{\delta z(t_0)} & \frac{\delta x(t)}{\delta \dot{x}(t_0)} & \frac{\delta x(t)}{\delta \dot{y}(t_0)} & \frac{\delta x(t)}{\delta \dot{z}(t_0)} \\ \frac{\delta y(t)}{\delta x(t_0)} & \frac{\delta y(t)}{\delta y(t_0)} & \frac{\delta y(t)}{\delta z(t_0)} & \frac{\delta y(t)}{\delta \dot{x}(t_0)} & \frac{\delta y(t)}{\delta \dot{y}(t_0)} & \frac{\delta y(t)}{\delta \dot{z}(t_0)} \\ \frac{\delta z(t)}{\delta x(t_0)} & \frac{\delta z(t)}{\delta y(t_0)} & \frac{\delta z(t)}{\delta z(t_0)} & \frac{\delta z(t)}{\delta \dot{x}(t_0)} & \frac{\delta z(t)}{\delta \dot{y}(t_0)} & \frac{\delta z(t)}{\delta \dot{z}(t_0)} \\ \frac{\delta \dot{x}(t)}{\delta x(t_0)} & \frac{\delta \dot{x}(t)}{\delta y(t_0)} & \frac{\delta \dot{x}(t)}{\delta z(t_0)} & \frac{\delta \dot{x}(t)}{\delta \dot{x}(t_0)} & \frac{\delta \dot{x}(t)}{\delta \dot{y}(t_0)} & \frac{\delta \dot{x}(t)}{\delta \dot{z}(t_0)} \\ \frac{\delta \dot{y}(t)}{\delta x(t_0)} & \frac{\delta \dot{y}(t)}{\delta y(t_0)} & \frac{\delta \dot{y}(t)}{\delta z(t_0)} & \frac{\delta \dot{y}(t)}{\delta \dot{x}(t_0)} & \frac{\delta \dot{y}(t)}{\delta \dot{y}(t_0)} & \frac{\delta \dot{y}(t)}{\delta \dot{z}(t_0)} \\ \frac{\delta \dot{z}(t)}{\delta x(t_0)} & \frac{\delta \dot{z}(t)}{\delta y(t_0)} & \frac{\delta \dot{z}(t)}{\delta z(t_0)} & \frac{\delta \dot{z}(t)}{\delta \dot{x}(t_0)} & \frac{\delta \dot{z}(t)}{\delta \dot{y}(t_0)} & \frac{\delta \dot{z}(t)}{\delta \dot{z}(t_0)} \end{bmatrix} \equiv \mathbf{\Phi}_{FD}(t,t_0) \tag{44}$$

Let the $N = 6$ test particle trajectories in the Poincaré integral invariant approach be equivalent to the initial state perturbations at t_0 used in the above finite difference method, i.e. Eq. 27 at t_0 becomes

$$\mathbf{\Omega}(t_0) = \text{diag}\left(\begin{bmatrix} -\delta\dot{x}_1(t_0) & -\delta\dot{y}_2(t_0) & -\delta\dot{z}_3(t_0) & \delta x_4(t_0) & \delta y_5(t_0) & \delta z_6(t_0) \end{bmatrix}\right) \tag{45}$$

and therefore

$$\mathbf{\Omega}^{-1}(t_0) = \text{diag}\left(\begin{bmatrix} -\delta\dot{x}_1^{-1}(t_0) & -\delta\dot{y}_2^{-1}(t_0) & -\delta\dot{z}_3^{-1}(t_0) & \delta x_4^{-1}(t_0) & \delta y_5^{-1}(t_0) & \delta z_6^{-1}(t_0) \end{bmatrix}\right) \tag{46}$$

Also, now evaluate Eq. 27 at t for our $N = 6$ perturbed trajectories,

$$\mathbf{\Omega}(t) = \begin{bmatrix} -\delta\dot{x}_1(t) & -\delta\dot{y}_1(t) & -\delta\dot{z}_1(t) & \delta x_1(t) & \delta y_1(t) & \delta z_1(t) \\ -\delta\dot{x}_2(t) & -\delta\dot{y}_2(t) & -\delta\dot{z}_2(t) & \delta x_2(t) & \delta y_2(t) & \delta z_2(t) \\ -\delta\dot{x}_3(t) & -\delta\dot{y}_3(t) & -\delta\dot{z}_3(t) & \delta x_3(t) & \delta y_3(t) & \delta z_3(t) \\ -\delta\dot{x}_4(t) & -\delta\dot{y}_4(t) & -\delta\dot{z}_4(t) & \delta x_4(t) & \delta y_4(t) & \delta z_4(t) \\ -\delta\dot{x}_5(t) & -\delta\dot{y}_5(t) & -\delta\dot{z}_5(t) & \delta x_5(t) & \delta y_5(t) & \delta z_5(t) \\ -\delta\dot{x}_6(t) & -\delta\dot{y}_6(t) & -\delta\dot{z}_6(t) & \delta x_6(t) & \delta y_6(t) & \delta z_6(t) \end{bmatrix} \tag{47}$$

Given Eq. 37, we premultiply Eq. 47 with Eq. 46 to yield

$$\mathbf{\Phi}_P^{-1}(t,t_0) = \begin{bmatrix} \frac{\delta\dot{x}_1(t)}{\delta\dot{x}_1(t_0)} & \frac{\delta\dot{y}_1(t)}{\delta\dot{x}_1(t_0)} & \frac{\delta\dot{z}_1(t)}{\delta\dot{x}_1(t_0)} & -\frac{\delta x_1(t)}{\delta\dot{x}_1(t_0)} & -\frac{\delta y_1(t)}{\delta\dot{x}_1(t_0)} & -\frac{\delta z_1(t)}{\delta\dot{x}_1(t_0)} \\ \frac{\delta\dot{x}_2(t)}{\delta\dot{y}_2(t_0)} & \frac{\delta\dot{y}_2(t)}{\delta\dot{y}_2(t_0)} & \frac{\delta\dot{z}_2(t)}{\delta\dot{y}_2(t_0)} & -\frac{\delta x_2(t)}{\delta\dot{y}_2(t_0)} & -\frac{\delta y_2(t)}{\delta\dot{y}_2(t_0)} & -\frac{\delta z_2(t)}{\delta\dot{y}_2(t_0)} \\ \frac{\delta\dot{x}_3(t)}{\delta\dot{z}_3(t_0)} & \frac{\delta\dot{y}_3(t)}{\delta\dot{z}_3(t_0)} & \frac{\delta\dot{z}_3(t)}{\delta\dot{z}_3(t_0)} & -\frac{\delta x_3(t)}{\delta\dot{z}_3(t_0)} & -\frac{\delta y_3(t)}{\delta\dot{z}_3(t_0)} & -\frac{\delta z_3(t)}{\delta\dot{z}_3(t_0)} \\ -\frac{\delta\dot{x}_4(t)}{\delta x_4(t_0)} & -\frac{\delta\dot{y}_4(t)}{\delta x_4(t_0)} & -\frac{\delta\dot{z}_4(t)}{\delta x_4(t_0)} & \frac{\delta x_4(t)}{\delta x_4(t_0)} & \frac{\delta y_4(t)}{\delta x_4(t_0)} & \frac{\delta z_4(t)}{\delta x_4(t_0)} \\ -\frac{\delta\dot{x}_5(t)}{\delta y_5(t_0)} & -\frac{\delta\dot{y}_5(t)}{\delta y_5(t_0)} & -\frac{\delta\dot{z}_5(t)}{\delta y_5(t_0)} & \frac{\delta x_5(t)}{\delta y_5(t_0)} & \frac{\delta y_5(t)}{\delta y_5(t_0)} & \frac{\delta z_5(t)}{\delta y_5(t_0)} \\ -\frac{\delta\dot{x}_6(t)}{\delta z_6(t_0)} & -\frac{\delta\dot{y}_6(t)}{\delta z_6(t_0)} & -\frac{\delta\dot{z}_6(t)}{\delta z_6(t_0)} & \frac{\delta x_6(t)}{\delta z_6(t_0)} & \frac{\delta y_6(t)}{\delta z_6(t_0)} & \frac{\delta z_6(t)}{\delta z_6(t_0)} \end{bmatrix} \tag{48}$$

Eq 48 can be rewritten as

$$\mathbf{\Phi}_P^{-1}(t,t_0) = \begin{bmatrix} \mathbf{\Phi}_{vv}^T & -\mathbf{\Phi}_{rv}^T \\ -\mathbf{\Phi}_{vr}^T & \mathbf{\Phi}_{rr}^T \end{bmatrix} \tag{49}$$

which brings us to the same result as Eqs. 42 and 43. Thus, the STM in Eq. 48 is rearranged in block component form to arrive at the same result as Eq. 44, thereby showing the two STM formulations to be equivalent for this choice of test particles (Case B).

Perturbation Size

We have not yet discussed the size of the perturbations δx and $\delta \dot{x}$ used to define the test particles, in both the Poincaré and finite difference approaches. Of course, the approximation of the partial derivatives in Eq. 44 would require small perturbations (but not so small as to result in numerical issues). However, as we discussed around Fig. 3, the triangle represents a locus of points and does not care if it is large or small. There is likely to be some connection between the size of the triangle and the "amount" that it deviates from a triangle as the locus of points evolves in phase space over time, but that is not explored in the present paper. We discuss the effect of perturbation size in the numerical tests to follow.

The Other Integral Invariants

We hinted earlier that there were reasons for mostly ignoring the other Poincaré integral invariants, I_4 and I_6 in the present paper. One reason is that the evaluation of the determinant in Eq. 15 is very simple for a 2-simplex, as we have seen for the triangle, but becomes much more complicated for a 4-simplex or a 6-simplex. Note that because of the multilinear property of the determinant, the 4-simplex and 6-simplex determinants can still be written as a linear function of the unknown state $\delta\mathbf{x}$, but with many more terms. Another reason for ignoring the higher dimensional invariants is because of the large number of test particles required. Recall that I_2 requires $N = 2n = 6$ test particles. In the case of I_4, we require $N = 3(2n) = 18$ test particles, because each row making up $\mathbf{y}$ is now a 4-D volume, where one of the vertices is our state of interest $\delta\mathbf{x}$. Each test particle must be unique. Particles cannot be reused between rows of $\mathbf{y}$; doing so would make the rows of $\mathbf{\Omega}$ linearly dependent, and therefore $\mathbf{\Omega}^{-1}$ would not exist. Likewise, I_6 would require $N = 5(2n) = 30$ test particles. We have used the symbolic library sympy in python to find expressions for these determinants, and they contain a large number of terms. For example, computing a *single* element in the matrix $\mathbf{\Omega}$ for I_4 requires 11 additions and 24 multiplications, and for I_6 requires 119 additions and 480 multiplications.

Discussion on Error

Until now, we have not spent much time discussing the error $\boldsymbol{\epsilon}$ appearing in Eq. 28. It should be noted that we have restricted the discussion to conservative Hamiltonian systems, to ensure that phase space volume, and the Poincaré integral invariants, are conserved. In fact, we can apply the new STM to nonconservative systems with ease, because the error term $\boldsymbol{\epsilon}$ will soak up the change in phase space volume. Note that the integration time steps between t_0 and t is usually small enough that any change in volume due to nonconservative forces will be negligible. In our preliminary numerical experiments described below, we apply the new STM to nonconservative systems to test its effectiveness.

NUMERICAL EXPERIMENTS

We can do some simple numerical experiments to see how the new Poincaré STM formulation compares with other methods for calculating the STM. Let's consider a satellite with initial orbital elements listed in Table 1. The numerical experiments consider two settings in the force model: one

that considers only conservative forces (gravitational potential from the Sun, Moon, and a 10-by-10 Earth spherical harmonic model), and one that adds nonconservative forces from solar radiation pressure (SRP) and atmospheric drag. Because the perigee altitude shown in Table 1 is well within the atmosphere, and the satellite area-to-mass ratio is set to 0.1 m^2 kg^{-1}, we can expect the nonconservative drag force to have a non-negligible impact on the orbit. The reference orbit is propagated using a Runge-Kutta 7(8) numerical integrator with an error tolerance of 1×10^{-13} and a variable step size. The experiments compare the STMs from both the new 2-D Poincaré STM formulation ($\mathbf{\Phi}_{\text{P}}$), the forward finite difference ($\mathbf{\Phi}_{\text{FD}}$), and from integrating the variational equations ($\mathbf{\Phi}_{\text{Var}}$). The commercial software FreeFlyer® version 7.6.0 is used to propagate the reference and truth orbits and to report out $\mathbf{\Phi}_{\text{Var}}$ that is integrated from the variational equations along the reference.

Table 1. Initial Orbital Elements

Perigee alt., km	Apogee alt., km	a, km	e	i, deg	Ω, deg	ω, deg	ν, deg
500 km	10000 km	11628	0.4	45	25	100	300

The flow of the numerical simulation is described in Fig. 4. The initial conditions for the reference state $\mathbf{x}^*$, an initial Gaussian uncertainty represented by a covariance matrix $\mathbf{P}_0$, a small deviation state $\delta\mathbf{x}$, and the initial test particle perturbations $\delta\mathbf{x}_i$ are first defined. The initial uncertainty $\mathbf{P}_0$ is defined as a diagonal matrix, with each position and velocity component having 1σ variances of 10 m and 0.1 mm s^{-1}, respectively. The initial deviation state is defined using the 1σ variances as $\delta\mathbf{x}(t_0) = (10, 10, 10, 0.1, 0.1, 0.1)$ m and mm s^{-1}. The orbit is propagated for 1 day. At each propagation time step, $\mathbf{\Phi}_{\text{P}}$ and $\mathbf{\Phi}_{\text{FD}}$ are computed from the integrated test particle trajectories. The STM $\mathbf{\Phi}_{\text{Var}}$ is integrated along with the equations of motion using the built-in methods from FreeFlyer®. Each STM is tested by using it to linearly propagate a small deviation state $\delta\mathbf{x}_{\text{STM}}$, where "STM" corresponds to each of the Poincaré, finite difference, and variational equation STMs. Likewise, $\mathbf{P}$ is linearly propagated with each STM. The state error $\mathbf{x}_{\text{err}}$, which is the difference between the linearly propagated state and the state from the Runge-Kutta integrator, is saved at each time step.

Tables 2 and 3, as well as Fig. 5 to 8, summarize the results of the numerical experiment. The position error columns in Table 2 come from $\mathbf{x}_{\text{err}}$, where we've computed the the mean of the position error vector norm of $\mathbf{x}_{\text{err}}$ over the entire 1 day time span. Table 3 of position uncertainty shows $\sqrt{\text{trace}(\mathbf{P})}$ at the end of the simulation. The column denoted "Monte Carlo" in Table 3 is computed from a point cloud of 1000 samples, drawn from the initial Gaussian distribution and propagated with the Runge-Kutta integrator. All numerical results use the Case B perturbations, because they were found to be nearly identical to the results using the Case A configuration.

Table 2. Test results, mean position error

		Test Particle Perturb.	Mean Position Error, km		
Num.	Forces	δx_i [km], $\delta \dot{x}_i$ [km/s]	Poincaré	Finite Diff.	Var. Eqns.
1	Cons.	1E-3, 1E-6	4.00E-4	4.00E-4	3.99E-4
2	Cons.	10, 0.1	0.12	0.12	3.99E-4
3	Noncons.	1E-3, 1E-6	diverge	diverge	0.22
4	Noncons.	10, 0.1	0.18	0.18	0.22

In tests 1 and 2, we have turned off the nonconservative drag and SRP forces; the numerical results show that, as expected the Poincaré and finite difference methods are nearly identical, as we showed them to be mathematically equivalent. Interestingly, the numerical results also show these two

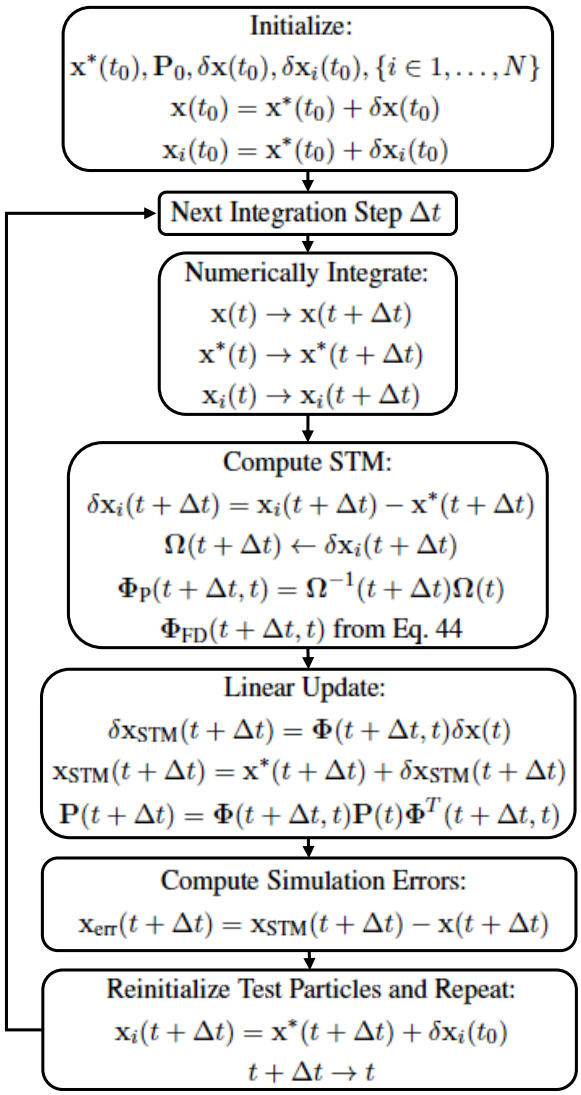

Figure 4. Illustration of the test process used in the numerical experiment.

Table 3. Test results, position uncertainty from $\sqrt{\mathrm{trace}(\mathbf{P})}$ after 1 day

		Test Particle Perturb.	Final Position 1σ Uncertainty, km			
Num.	Forces	δx_i [km], $\delta \dot{x}_i$ [km/s]	Poincaré	Finite Diff.	Var. Eqns.	Monte Carlo
1	Cons.	1E-3, 1E-6	3.123	3.123	3.123	3.165
2	Cons.	10, 0.1	3.522	3.522	3.123	3.165
3	Noncons.	1E-3, 1E-6	diverge	diverge	3.134	3.176
4	Noncons.	10, 0.1	3.923	3.923	3.134	3.176

methods to have nearly identical performance even in tests 3 and 4 when the nonconservative forces are turned on, despite the fact that our mathematical proof assumes a conservative Hamiltonian system between times t and $t + \Delta t$.

With only conservative forces and small perturbations (test 1, Fig. 5), we see nearly identical

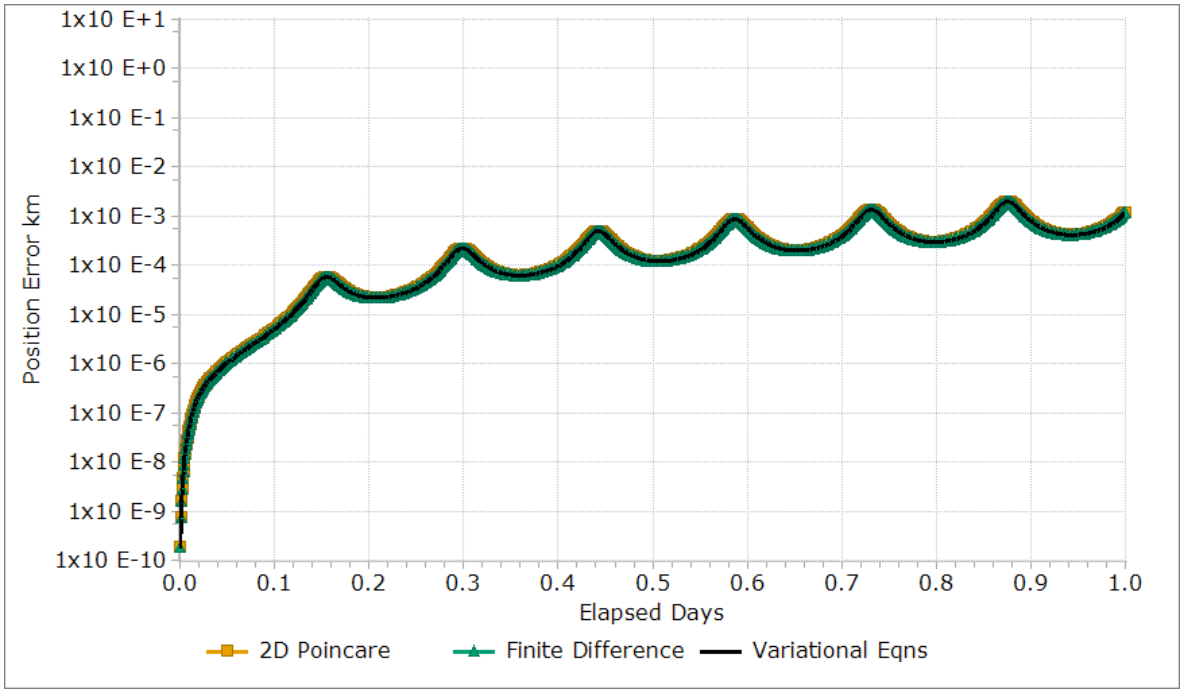

Figure 5. Test 1 position error, conservative forces with small test particle perturbations. Note that all data are nearly identical and plotted on top of one another.

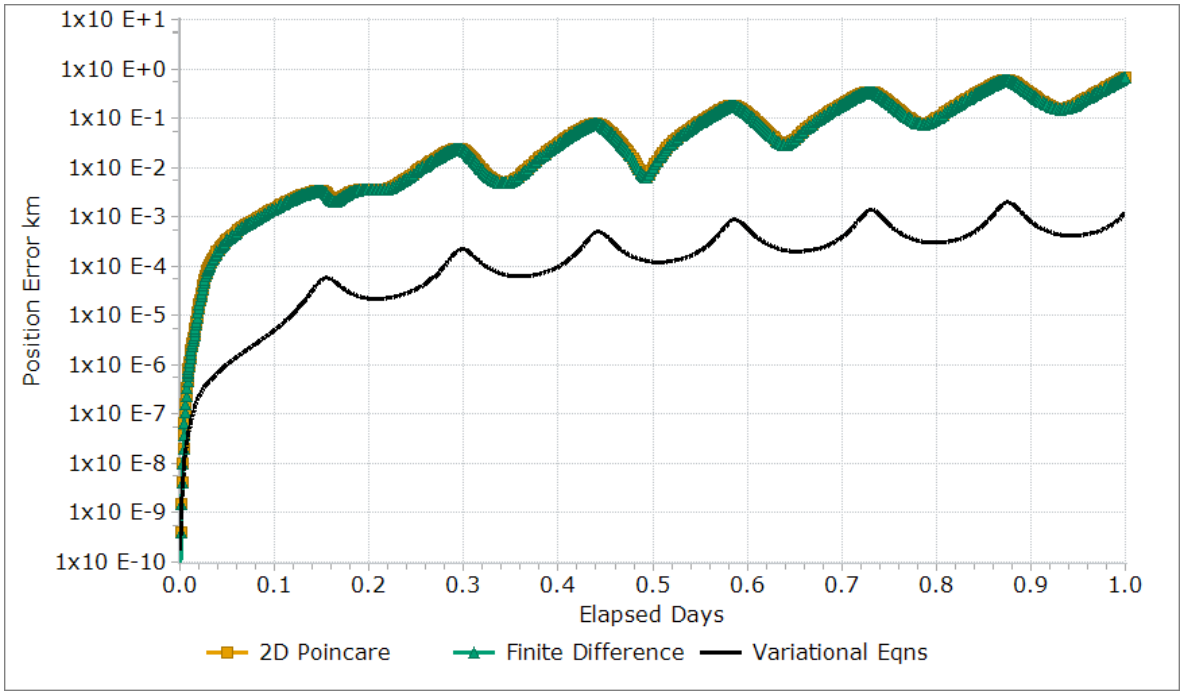

Figure 6. Test 2 position error, conservative forces with large test particle perturbations. Note that Poincaré and finite difference series are nearly identical and plotted on top of one another.

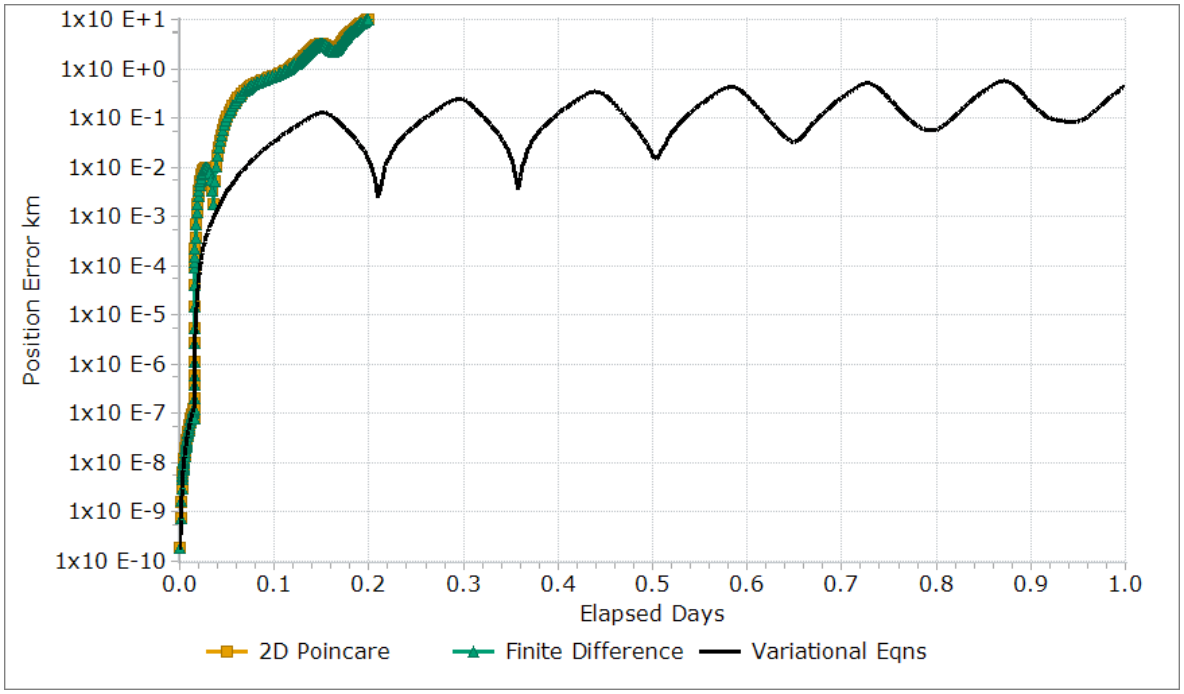

Figure 7. Test 3 position error, nonconservative forces with small test particle perturbations. The Poincaré and finite difference methods quickly diverge.

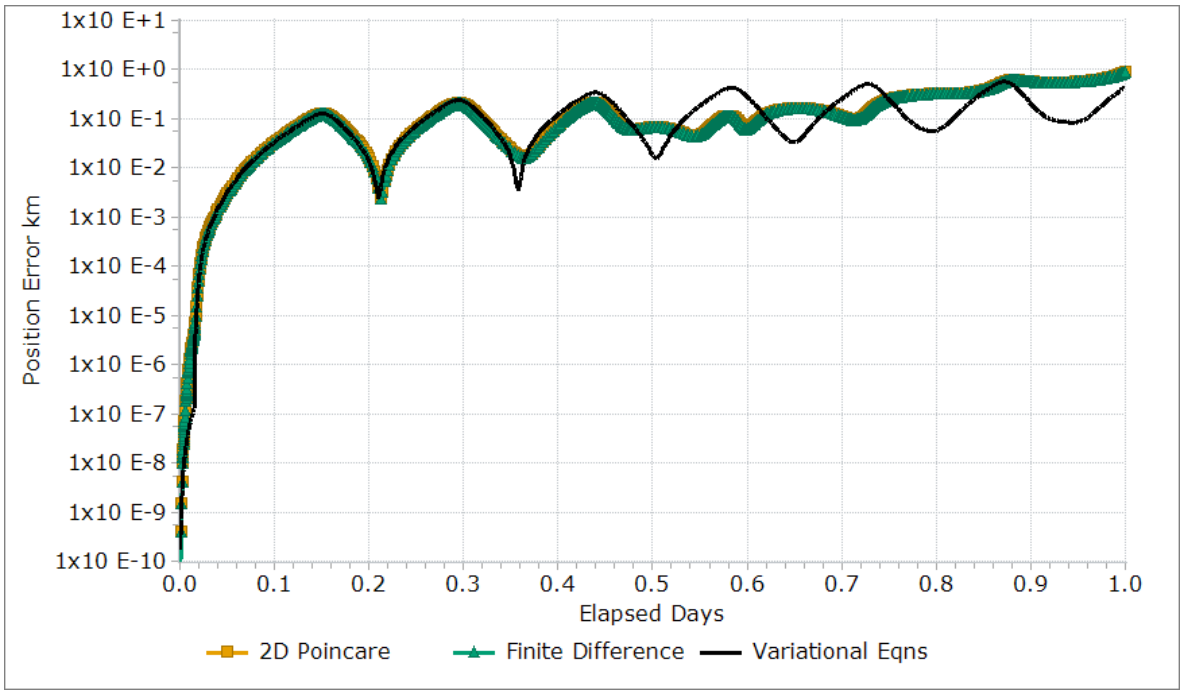

Figure 8. Test 4 position error, nonconservative forces with large test particle perturbations. The Poincaré and finite difference methods have somewhat similar performance as the variational equations over this test span.

performance between all methods. This could be due to the slowly changing nature of the dynamics for this particular orbit, suggesting that the linearization is not sensitive to the method used. Test 2 in Figure 6 is a nearly identical setup to the first test, but we've increased the size of the test particle perturbations δx_i and $\delta \dot{x}_i$. We can see that the performance gets worse (error grows) when we increase the size of the test particle perturbations, as we would expect from the finite difference.

In tests 3 and 4 we have turned on the nonconservative forces; we can no longer prove mathematically that the Poincaré and finite different methods are equivalent, as the derivation around Eq. 48 assumed sympletic matrices. We see in test 3 that when the test particle perturbations δx_i and $\delta \dot{x}_i$ are small, the errors diverge after a short amount of time, as the spacecraft reaches the first perigee dip into the atmosphere (recall from Table 1 the initial true anomaly ν places the spacecraft shortly before perigee). In test 4, the performance is improved by increasing the size of the test particle perturbations, such that Poincaré and finite different methods have similar performance to the variational equations. In fact, for this particular experimental setup, the mean position error is slightly smaller (0.18 km) when using $\mathbf{\Phi}_{\text{P}}$ or $\mathbf{\Phi}_{\text{FD}}$ compared with 0.22 km with $\mathbf{\Phi}_{\text{Var}}$.

Comparing Fig. 7 and 8 with Fig. 5 and 6, we can see that the linearization error from Φ_{Var} grows when the nonconservative drag force is added; this illustrates the highly nonlinear effects around perigee as the spacecraft dips into the atmosphere, even when the variational equations are used. Also, an interesting result is that the finite difference method in test 4 performs well, despite the fact that the finite difference approximation of the partial derivatives assumes small perturbations to the reference trajectory. Although we haven't proven that the FD and Poincaré methods are mathematically equivalent when including nonconservative forces, this numerical result suggests that the two approaches yield nearly identical results, and may benefit from larger perturbations when the system is sufficiently nonlinear.

Table 3 shows that for all tests, the propagation of the covariance matrix was identical between $\mathbf{\Phi}_{\text{P}}$ and $\mathbf{\Phi}_{\text{FD}}$. Also, among the various tests, the position uncertainty from the computed covariance is similar magnitude to that computed from both the variational equations and from the full Monte Carlo. Of course, because this is only a linear propagation of $\mathbf{P}$, we would expect the errors compared with the Monte Carlo to grow over time, especially in test 4 with the addition of the drag and SRP forces that exacerbate the nonlinear dynamics.

The results in this study show the potential for examining the linearization error in astrodynamical problems through the lens of Hamiltonian dynamics, as we have equated the error term $\boldsymbol{\epsilon}$ in Eq. 28 to the change in the computed Poincaré integral invariants over time. The understanding developed in this paper may be useful to others wishing to explore new methods for linearization or uncertainty propagation. From a computational standpoint, the new numerical method shown in this paper requires the same number of satellite propagations as integrating the variational equations; $N = 6$ test particles, along with the reference trajectory, resulting in 42 states needing numerical integration. The benefit of the numerical methods, both the Poincaré and the finite difference, is that the partial derivatives of the accelerations need not be computed. Of course, the disadvantage of the numerical methods is the need to choose a suitable perturbation of the test particles relative to the reference. The present study gives a new understanding that large perturbations are mathematically acceptable, and in some cases may actually improve performance, especially for highly nonlinear systems.

CONCLUSION

The Poincaré integral invariants were examined and used to derive a new STM that is formed numerically by integrating test particles along with the reference trajectory. This paper focused on the 2-D invariant, as the formulation was shown to much simpler, although in principle the 4-D and 6-D invariants can also be used, but at a higher computational cost. The method using the 2-D invariant was shown to be equivalent to the forward finite difference method for computing the STM. Numerical results were presented that demonstrated the equivalence between the Poincaré method and the forward finite difference. Also, despite the new method assuming conservative Hamiltonian dynamics on the time-scale of an integration time step, we demonstrated that it can be applied to nonconservative systems and still have similar performance as integrating the variational equations, albeit over shorter analysis time spans.

ACKNOWLEDGMENT

The first author wishes to thank Benjamin Villac for introducing him to the Poincaré integral invariants many years ago.

NOTATION

$\boldsymbol{\epsilon}$	error vector	k	index, also dimension of simplex
ν	true anomaly	L	Lagrangian
$\mathbf{\Phi}$	state transition matrix	M	manifold
$\mathbf{\Omega}$	intermediate matrix quantity	N	number of test particles
Ω	right-ascension of ascending node	n	degrees of freedom
ω	argument of perigee	$\mathbf{O}$	zero matrix
A	phase-space area (volume)	$\mathbf{P}$	covariance matrix
a	semi-major axis	$\mathbf{p}$	conjugate momenta
$\mathcal{B}_n$	n-dimensional set in phase space	$\mathbf{q}$	generalized coordinates
e	eccentricity	$\mathbb{R}$	set of real numbers
H	Hamiltonian	T	kinetic energy
$\mathbf{I}$	identity matrix	t	time
i	index, also inclination	V	potential energy
I_2	2-D Poincaré integral invariant	$\mathbf{v}$	vertex vector
I_4	4-D Poincaré integral invariant	$\mathbf{x}$	state vector
I_6	6-D Poincaré integral invariant	$\mathbf{x}^*$	reference state vector
J	symplectic matrix	$\delta\mathbf{x}$	relative state vector
		$\mathbf{y}$	vector of invariants

APPENDIX A

The new STM defined by Eq. 31 can be shown to satisfy the following three properties. The identity property:

$$\mathbf{\Phi}(t_0, t_0) = \mathbf{I}_{N\times N} \tag{50}$$

$$\mathbf{\Omega}^{-1}(t_0)\mathbf{\Omega}(t_0) = \mathbf{I}_{N\times N} \tag{51}$$

The inverse property:

$$\mathbf{\Phi}(t_0, t) = \mathbf{\Phi}^{-1}(t, t_0) \tag{52}$$

$$\mathbf{\Omega}^{-1}(t_0)\mathbf{\Omega}(t) = [\mathbf{\Omega}^{-1}(t)\mathbf{\Omega}(t_0)]^{-1} \tag{53}$$

$$= \mathbf{\Omega}^{-1}(t_0)\mathbf{\Omega}(t) \tag{54}$$

The commutative property:

$$\mathbf{\Phi}(t_2, t_0) = \mathbf{\Phi}(t_2, t_1)\mathbf{\Phi}(t_1, t_0) \tag{55}$$

$$\mathbf{\Omega}^{-1}(t_2)\mathbf{\Omega}(t_0) = \mathbf{\Omega}^{-1}(t_2)\mathbf{\Omega}(t_1)\mathbf{\Omega}^{-1}(t_1)\mathbf{\Omega}(t_0) \tag{56}$$

$$= \mathbf{\Omega}^{-1}(t_2)\mathbf{\Omega}(t_0) \tag{57}$$

REFERENCES

[1] E. Pellegrini and R. Russell, "On the Computation and Accuracy of Trajectory State Transition Matrices," *Journal of Guidance, Control, and Dynamics*, Vol. 39, 2016, pp. 2485–2499.

[2] D. Scheeres, F.-Y. Hsiao, R. Park, B. Villac, and J. Maruskin, "Fundamental limits on spacecraft orbit uncertainty and distribution propagation," *The Journal of the Astronautical Sciences*, Vol. 54, 2006, pp. 505–523.

[3] D. Scheeres, M. de Gosson, and J. Maruskin, "Applications of Symplectic Topology to Orbit Uncertainty and Spacecraft Navigation," *The Journal of the Astronautical Sciences*, Vol. 59, 2012, pp. 63–83.

[4] O. Boodram and D. Scheeres, "Constrained evolution of Hamiltonian phase space distributions in the presence of natural, non-conservative forces," *Celestial Mechanics and Dynamical Astronomy*, Vol. 136, 2024.

[5] O. Boodram and D. Scheeres, "Targeting Hamiltonian Integral Invariant Behaviour with Control to Manipulate Spacecraft Phase Space Distributions," *AAS/AIAA Astrodynamics Specialist Conference*, Big Sky, MT, 2023.

[6] T. Jordan, "Steppingstones in Hamiltonian dynamics," *American Journal of Physics*, Vol. 72, 2004, pp. 1095–1099.

[7] V. Arnold, *Mathematical Methods of Classical Mechanics, 2nd ed.*, ch. 9, pp. 237–239. New York, NY: Springer, 1989.

[8] O. Montenbruck and E. Gill, *Satellite Orbits: Models, Methods, Applications, 3rd ed.*, ch. 7, p. 239. New York, NY: Springer, 2005.